Application of *MAT_258 for Bending and Crushing of Extruded Aluminum Profiles Using Shell Elements

Jens Kristian Holmen[1], Joakim Johnsen[1], David Morin[2,3], Tore Børvik[2,3], Magnus Langseth[2,3]
[1]Enodo AS, Trondheim, Norway
[2]Structural Impact Laboratory (SIMLab), Department of Structural Engineering, Norwegian University of Science and Technology (NTNU), Trondheim, Norway
[3]Centre for Advanced Structural Analysis (SFI CASA), NTNU, Trondheim, Norway

Abstract

**MAT_258 (*MAT_NON_QUADRATIC_FAILURE) is a through-thickness failure regularization model for shells in LS-DYNA®. In this model the failure parameter is computed as a function of the size of the element as well as its bending-to-membrane loading ratio. The constitutive behavior and fracture surface in *MAT_258 are represented by well-known analytical expressions which simplify the calibration process. This means that ductile failure initiation can be predicted in thin-walled metallic structures with minimal calibration effort and cost. In this study, we go through the calibration process of *MAT_258 for two aluminum alloys before the calibrated material cards are applied in shell element simulations of double-chamber aluminum extrusions in both three-point bending and crushing.*

Introduction

Shell elements can correctly predict the elastic-plastic behavior of thin-walled metallic structures up to quite significant strains. Failure prediction, on the other hand, remains a modeling challenge. Usually, the element size is larger than the width of a diffuse neck, meaning that the spatial evolution of the necking instability cannot be correctly represented. Furthermore, after the subsequent local necking, the plane stress assumption no longer applies, and the finite element solution becomes increasingly dependent on the element size.

Another issue is that sheet metals generally exhibit a much higher structural ductility when they are subjected to bending than when they are subjected to membrane stretching since bending does not trigger local necking. This issue is important for shell elements and must be kept int mind for material models where the failure criterion is regularized based on element size. A regularization scheme accounting for membrane stretching alone might predict premature failure if the material is subjected to bending.

One to three calibration tests are necessary to generate a *MAT_258 material card. The material card consists of relatively few, physically based parameters that each have a clear purpose. It is important for the robustness of the material model that the parameters are not unnecessarily convoluted. The most important feature of *MAT_258 is that the model treats fracture due to bending and fracture due to membrane stretching separately so that large shell element models can be used to predict fracture at the correct point in time for both bending dominated and membrane dominated stress states. In the following, the simplest form of *MAT_258 is calibrated from a single tension test before it is evaluated on a macroscopic scale.

Model description

*MAT_258 (*MAT_NON_QUADRATIC_FAILURE) is an isotropic elastic-viscoplastic model with a non-quadratic yield surface [1][2]. Strain-rate sensitivity can be invoked using a modified Johnson-Cook type viscoplastic relation [3][4], but this feature was not used in this work. Failure is uncoupled from the constitutive behavior, but is dependent on both the stress state, the deformation mode, and the size of the elements.

The equivalent stress is defined as

$$\bar{\sigma} = \left[\frac{1}{2}(|\sigma_1 - \sigma_2|^a + |\sigma_2 - \sigma_3|^a + |\sigma_3 - \sigma_1|^a)\right]^{\frac{1}{a}} \tag{1}$$

where $\sigma_1 > \sigma_2 > \sigma_3$ are the ordered principal stresses and a controls the shape of the yield surface. For $a = 2$, Eq. (1) is identical to the von Mises yield surface. For $a = 1$ and $a \to \infty$, Eq. (1) represents Tresca's yield surface. It is customary to use $a = 6$ for body centered cubic materials (steel) and $a = 8$ for face centered cubic materials (aluminum) [5]. The hardening curve is defined by a three-term Voce expression as follows

$$\sigma_Y = \sigma_0 + R(\bar{\varepsilon}^{\mathrm{p}}) = \sigma_0 + \sum_{i=1}^{3} Q_i \left(1 - \exp\left(-\frac{\theta_i}{Q_i}\bar{\varepsilon}^{\mathrm{p}}\right)\right) \tag{2}$$

where σ_0 is the initial yield stress, Q_i and θ_i control the work hardening, and $\bar{\varepsilon}^{\mathrm{p}}$ is the equivalent plastic strain.

An uncoupled Extended Cockcroft-Latham (ECL) criterion [6] is implemented to evaluate failure. In its complete form, the failure indicator (damage parameter in LS-DYNA) evolves according to the following equation

$$\dot{D} = \frac{\bar{\sigma}}{W_C}\langle \phi \frac{\sigma_1}{\bar{\sigma}} + (1 - \phi)\left(\frac{\sigma_1 - \sigma_3}{\bar{\sigma}}\right)\rangle^{\gamma} \dot{\bar{\varepsilon}}^{\mathrm{p}} \tag{3}$$

where D is the failure indicator while the model parameters W_C, ϕ and γ control the damage evolution. Note the Macaulay brackets where $\langle x \rangle = \max(0, x)$. Because the criterion includes three parameters, it requires three different material tests for a complete calibration. In this work we have for simplicity calibrated the standard Cockcroft-Latham (CL) criterion [7] from a single tensile test. This can be obtained by setting $\phi = \gamma = 1$

$$\dot{D} = \frac{1}{W_C}\langle \sigma_1 \rangle \dot{\bar{\varepsilon}}^{\mathrm{p}} \tag{4}$$

Now the Lode parameter (L) dependence and stress triaxiality ratio (σ^*) dependence of the criterion are predetermined by Eq. (4) since σ_1 can be written as a function of L and σ^* [8].

When using shell elements and *MAT_258, the CL parameter (W_C) is comprised of the CL parameter in pure bending (W_C^{b}) which is independent of the mesh and the CL parameter in pure membrane loading (W_C^{m}) which is very mesh dependent. They are combined using the following function

$$W_C = \Omega W_C^{\mathrm{b}} + (1 - \Omega) W_C^{\mathrm{m}} \tag{5}$$

where Ω is the bending indicator which is 1 in pure bending and 0 in pure membrane, and is calculated as follows

$$\Omega = \frac{1}{2}\frac{\left|\varepsilon_{33}^{\mathrm{p}+} - \varepsilon_{33}^{\mathrm{p}-}\right|}{\max\left(\left|\varepsilon_{33}^{\mathrm{p}+}\right|, \left|\varepsilon_{33}^{\mathrm{p}-}\right|\right)} \tag{6}$$

Here, $\varepsilon_{33}^{\mathrm{p}+}$ and $\varepsilon_{33}^{\mathrm{p}-}$ are the through-thickness plastic strains on the two sides of the shell element. The bending CL parameter (W_C^{b}) is the same in every element, while the membrane CL parameter (W_C^{m}) is calculated as a function of the element size in the following way

$$W_C^{\mathrm{m}} = W_C^{\mathrm{l}} + \left(W_C^{\mathrm{s}} - W_C^{\mathrm{l}}\right)\exp\left(-c\left(\frac{l_{\mathrm{e}}}{t_{\mathrm{e}}} - 1\right)\right) \tag{7}$$

where W_C^{l}, W_C^{s}, and c are parameters that need to be calibrated while l_{e} and t_{e} are the characteristic side length and thickness of the shell element, respectively.

Material tests

Double-chamber extruded profiles made from two 6000-series aluminum alloys supplied by Hydro Extruded Solutions were used in this work. They will be referred to as Alloy A ($\sigma_0 \approx 255$ MPa) and Alloy B ($\sigma_0 \approx 317$ MPa). The outer dimensions of the cross-section of the profile are approximately 75 mm × 125 mm, while the wall thickness of the outer wall is 2.7 mm and the wall thickness of the web is 1.5 mm. Figure 1a shows the geometry of the test coupons that were extracted from the profiles. The material tests presented and used in the following are from the extrusion direction of the 2.7 mm thick outer wall. Note that an extruded aluminum profile usually is anisotropic due to its deformation-induced texture, but this is not considered in this work.

Figure 2 shows representative engineering stress-strain curves for the two materials. We conducted the tension tests in an Instron 5982 testing machine with a crosshead velocity of 0.34 mm/min which corresponds to an approximate initial strain rate of 0.0005 1/s. A black-and-white speckle pattern was painted on the surface of the specimen before testing. A Basler acA4112-30um camera photographed the tests at 1 Hz. The engineering stress was calculated based on the load cell in the machine ($\sigma_{\mathrm{e}} = F/A_0$) and the engineering strain was found from a global virtual extensometer that was approximately 8 mm long ($e = \Delta L/L_0$).

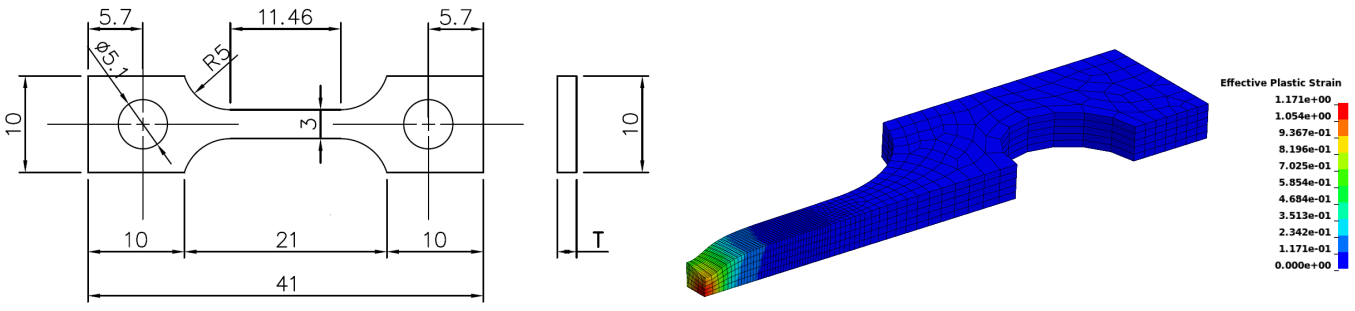

(a) (b)

Figure 1: (a) Geometry of the UT41 specimen and (b) fringe plot of the simulation used to calibrate W_C^{b} and the hardening curve.

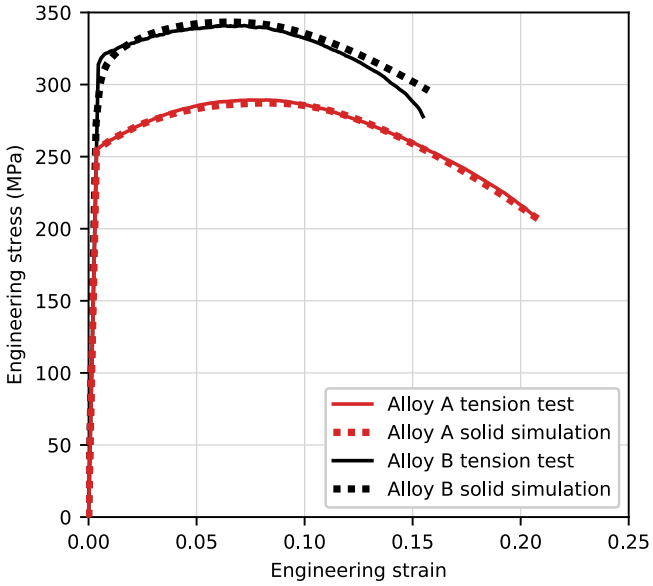

Figure 2: Engineering stress-strain curves for Alloy A and Alloy B from tension tests with an extensometer length $L \approx 8$ mm.

Component tests

Figure 3 shows the test setup for the two different types of component tests that were conducted: Crush tests and pre-notched three-point bending tests. The main reason for choosing these two test setups was to validate the material cards for different load types. The material in the crushing tests experience local buckling and consequently the elements are subjected to severe bending (see Figure 4). This will be used to make sure that the fracture criterion works as intended for severe bending loads. For the three-point bending tests, fracture first occurs in the notched part of the specimen, close to the notch root (see Figure 5). Here, the material experiences biaxial tension with almost no bending. This will be used to verify that the element size regularization works as intended for membrane loads.

In other words, we want to predict that the initial fracture occurs at the correct location at the correct time in the three-point bending tests, while predicting the correct amount of fracture in the crushing tests.

The crushing tests (five repetitions) were conducted in a hydraulic test machine with a crushing speed of 10 mm/min. Figure 3a shows a schematic of the crush tests. The total height of the tested profile was 430 mm and the compression distance was 250 mm. To ensure repeatable buckling shapes, a 9.915 mm trigger was made at the top of the profile. The profile was not clamped in the machine but held in place by friction between the platens and the specimen.

The three-point bending tests (five repetitions) were conducted in a universal test machine with a punch speed of 10 mm/min. Figure 3b shows a schematic of the three-point bend tests. The total length of the profile was 480 mm and a notch with radius 18 mm was placed with an eccentricity of 80 mm at the bottom of the profile. The distance between the supports was 375 mm and the diameter of the punch and supports was 60 mm. To limit frictional effects the punch and supports were covered in Teflon tape.

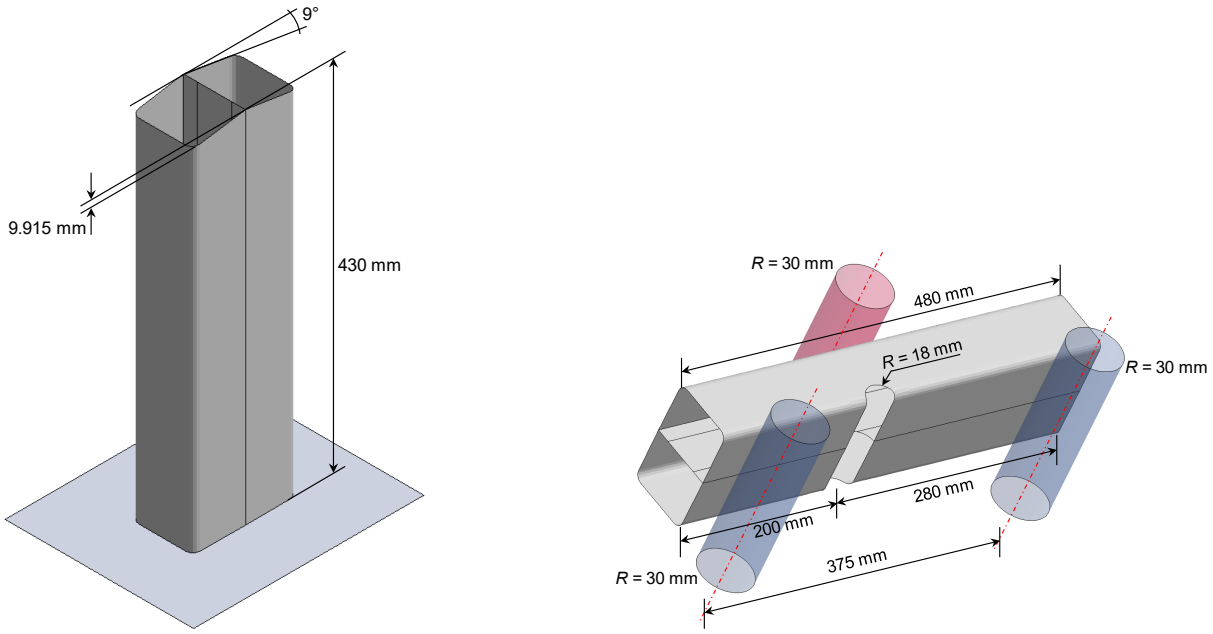

(a) (b)

Figure 3: Test setup of (a) the crush tests and (b) the three-point bending test.

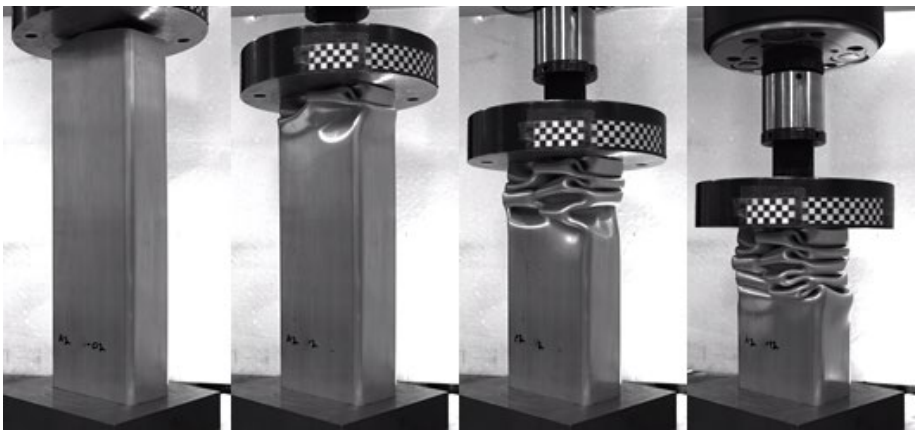

(a) Alloy A

(b) Alloy B

Figure 4: Images of the crushing behavior for (a) Alloy A and (b) Alloy B.

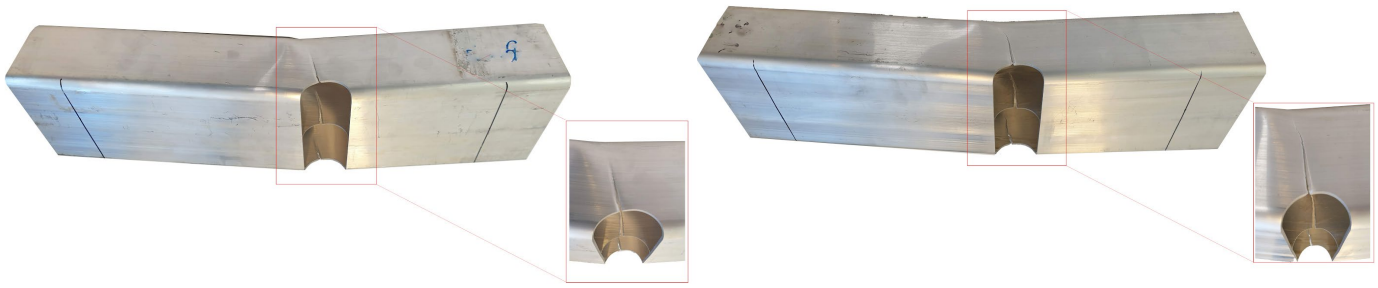

(a) Alloy A (b) Alloy B

Figure 5: Images of fractured three-point bending specimens for (a) Alloy A and (b) Alloy B.

Figures 4 and 5 show images from the tests. We see from the crushing tests that the Alloy A cracks to a lesser degree than the Alloy B profile. In Figure 5 we see that the fracture starts close to the notch root and that it propagates toward the symmetry line of the profile where the punch was located.

Figure 6a shows the force-displacement curves from the crush tests. Alloy B has a higher initial peak force and a higher sustained force than Alloy A. The scatter is also slightly larger for Alloy B. Figure 6b shows the force-displacement curves from the three-point bending tests. Alloy B exhibits overall higher forces, while the displacement at fracture is similar, and for some tests slightly higher than for Alloy A. Also, for the three-point bend tests, the scatter is larger for Alloy B than for Alloy A (both in force level and point of initial fracture).

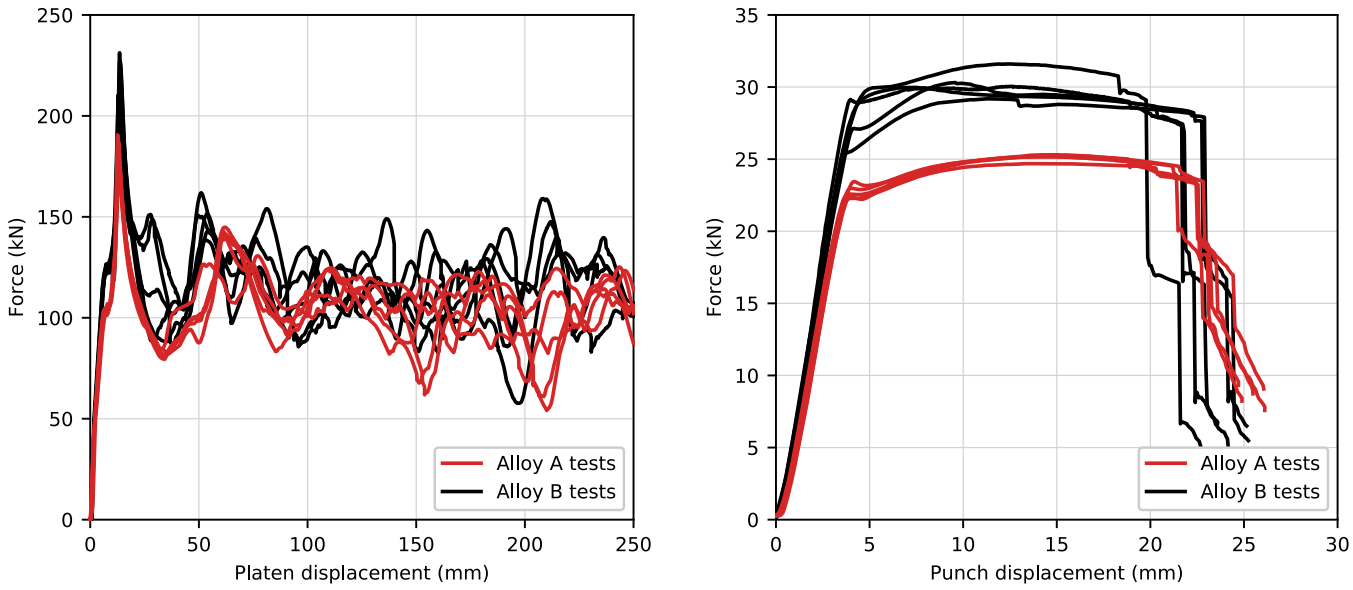

(a) Crush (b) Three-point bend

Figure 6: Force-displacement curves for (a) crush tests and (b) three-point bend tests of Alloy A and Alloy B.

Calibration procedure

Although *MAT_258 can represent strain rate sensitivity and includes a three-parameter Lode dependent failure criterion, we have chosen to calibrate the model in its simplest form. This means that $\phi = \gamma = 1$ in Eq. (3) such that we obtain the original CL criterion in Eq. (4). This was done to limit the number of material tests needed for calibration to a single test, and to show that even this simple calibration is enough to deal with many of the most important issues in simulations with shell elements.

Calibration of *MAT_258 is in this work based on a single dogbone tension test by using the following steps:

1. Conduct experimental test with speckle pattern for digital image correlation (DIC).
2. Use DIC to extract the elongation of a global virtual extensometer for the engineering stress-strain curve and several shorter virtual extensometers for element size regularization purposes.
3. Run an LS-OPT® analysis with a solid element model of the tension test (use e.g. *MAT_033). Use the force-displacement curve from the global virtual extensometer as the target to optimize the parameters in the isotropic hardening curve (σ_0, θ_i, Q_i) while the final run is used to calculate the failure parameter for bending deformation (W_C^{b}). The final simulations are included in Figure 2.
4. Single-element models (Figure 7) with applied boundary conditions from the shorter extensometers are run and the failure parameters for membrane deformation (W_C^{l}, W_C^{s}, c) are found.

Regarding points 1 and 2 from the list above: For the relatively small tensile test specimens shown in Figure 1 we used a global virtual extensometer with $L_0 \approx 8$ mm and smaller regularization virtual extensometers of lengths roughly between $l_{\mathrm{e}}/t_e = 1$ and $l_{\mathrm{e}}/t_e = 3$ (2.67 mm, 3.148 mm, 3.699 mm, 4.239 mm, and 6.939 mm for Alloy A). Regarding point 3 from the list above: The bending CL parameter was found by integrating the major principal stress σ_1 over the equivalent plastic strain from the central integration point in the solid element simulation as follows

$$W_C^{\mathrm{b}} = \int_0^{\bar{\varepsilon}_{\mathrm{f}}^{\mathrm{p}}} \sigma_1 \, \mathrm{d}\bar{\varepsilon}^{\mathrm{p}} \tag{8}$$

The integration stops at the timestep where the engineering strain, i.e., the extensometer displacement, is identical to the strain at fracture in the test. Regarding point 4 from the list above: Similarly, we prescribe the longitudinal displacement from the regularization extensometers to the single element models shown in Figure 7. A value for

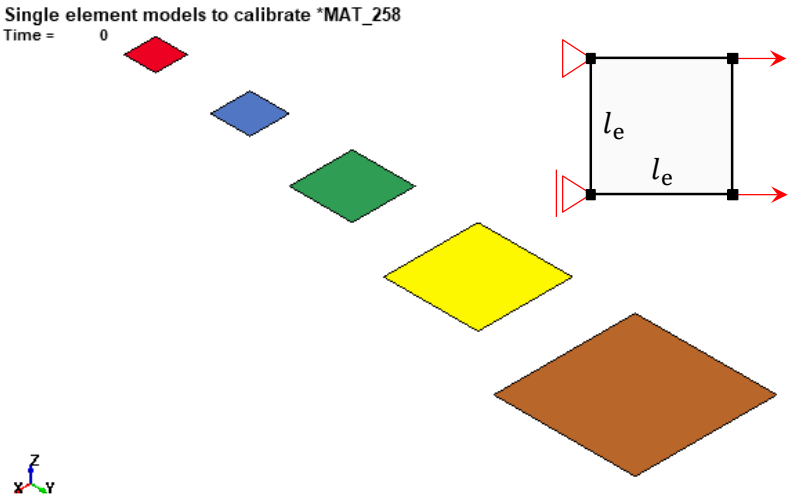

Figure 7: Single-element models from which the membrane CL parameter W_C^{m} is determined for different element sizes.

W_C^{m} is found for each element and these results are used to fit the parameters in Eq. (7). Figure 8a illustrates the membrane regularization and it shows the datapoint values for W_C^{m} and the curve fit. Note that we simplify the deformation of the single element models to be uniaxial stress.

Figure 8b illustrates the effect of the parameter Ω, and thus the effect of the bending-to-membrane ratio on the fracture strain for plane stress conditions. The fracture curve comes from the one-parameter CL failure criterion for proportional loading (see Gruben et al. [6] for details). A linear interpolation occurs in the code between pure bending ($\Omega = 1$) and pure membrane loading ($\Omega = 0$). For pure bending, the curve is constant regardless of the element size, but for pure membrane the curve changes according to Eq. (7).

The parameters in the regularized fracture criterion each have specific meanings: W_C^{b} (WCB in the manual) is the mesh independent CL failure parameter for pure bending, W_C^{l} (WCL) represents the membrane CL parameter for $l_{\mathrm{e}}/t_{\mathrm{e}} \to \infty$, W_C^{s} (WCS) represents the membrane CL parameter for $l_{\mathrm{e}}/t_{\mathrm{e}} = 1$, and c (CC) controls the slope of the element size regularization curve. The strain rate part of *MAT_258 is suppressed by setting the parameters CS = PDOTS = 0.0. The thickness of the part must be input as THICKNESS and is needed in simulations when ELFORM = 16 is used.

Component simulations

The calibrated material cards were used to simulate the component tests in LS-DYNA (Version R9.3.0). The model parameters are listed in Tables 1 and 2. We used various mesh densities to evaluate how well the regularization procedure works: Two different element sizes for the crush simulations (2.7 mm and 5.4 mm) and three different element sizes for the three-point bending simulations (2.7 mm, 4.0 mm and 5.4 mm). A characteristic element size of 5.4 mm ($l_{\mathrm{e}}/t_{\mathrm{e}} = 2$) was barely small enough to capture the deformation pattern in the crush tests.

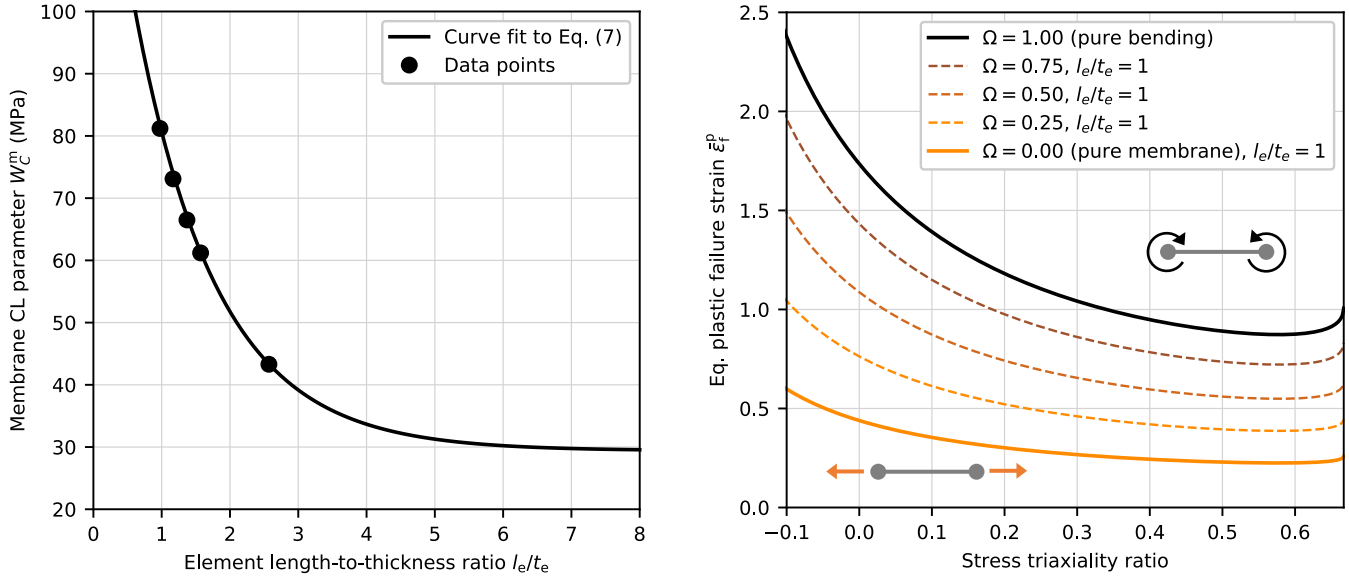

(a) (b)

Figure 8: Effects of (a) membrane regularization for different element sizes and (b) bending regularization for $l_{\mathrm{e}}/t_{\mathrm{e}} = 1$ on Alloy A. Note that the final CL parameter used in the simulation (W_C) is independent of the element size for pure bending, see Eq. (5).

To speed up the simulations we used a time scaling factor of 15 000 for crushing and 1800 for three-point bending test. Most of the simulations are conducted with the default element formulation ELFORM = 2 with 5 integration points over the thickness, but we also checked the results by using ELFORM = 16. The control settings for the component simulations are loosely based on a set of recommended settings for structural impact [9]. In the *CONTROL_SHELL card we used ISTUPD = 1, BWC = 1, PROJ = 1 and IRNXX = -1. We applied hourglass control type IHQ = 4 with QM = 0.03 and contact between different parts and self-contact was ensured with *CONTACT_AUTOMATIC_SINGLE_SURFACE with SOFT = 1 and VDC = 20 in all the simulations. Friction in the contact formulation was FD = FS = 0.2 in the crush simulations and FD = FS = 0.05 in the three-point bending simulations. Element erosion occurs when 2 out of the 5 integration points over the thickness reach the failure criterion.

Figure 9 shows crushed shapes of Alloy A and Alloy B. There are particularly two things that can be seen here. First, the Alloy A simulation exhibits ductile behavior with few visible cracks, while Alloy B exhibits some cracking in the corners and in the connection between the outer wall and web. Overall, this is consistent with the experiments shown in Figure 4. Second, the fringe plots show the bending parameter Ω (History Variable #4) and the parameter is (as expected) close to 1.0 in large parts of the profile, confirming that this test setup is bending dominated. Figure 10a shows the failure indicator (History Variable #2) for the three-point bending simulation just before first fracture. Comparing Figure 10b to Figure 10a shows that Ω is close to 0.0 where the failure indicator is highest, confirming that failure in this test setup is membrane dominated.

Force-displacement curves from the simulations are compared to tests in Figure 11 and 12. The crush simulations in Figure 11 show an overall good correspondence to the tests for both element sizes. The peak force is underestimated, but the average crush force level is acceptable which indicates that the amount of cracking is not overestimated in the simulation.

In Figure 12, we see that the point of first fracture in the three-point bending simulation is slightly overestimated for Alloy A and that first fracture occurs on the early side (within the experimental scatter) for Alloy B. For simulations with a characteristic element size of 2.7 mm and 4.0 mm the fracture displacement is almost identical, but when the element size is 5.4 mm the displacement at fracture is distinctly different both for Alloy A and Alloy B. One reason is that model only dampens the mesh sensitivity. Another is that the geometry of the notch and the rounded corners of the profile cannot be sufficiently represented by the coarse mesh. The latter is substantiated by the fact that the force is higher in simulations with 5.4 mm elements compared to 2.7 mm and 4.0 mm which will affect the point of fracture.

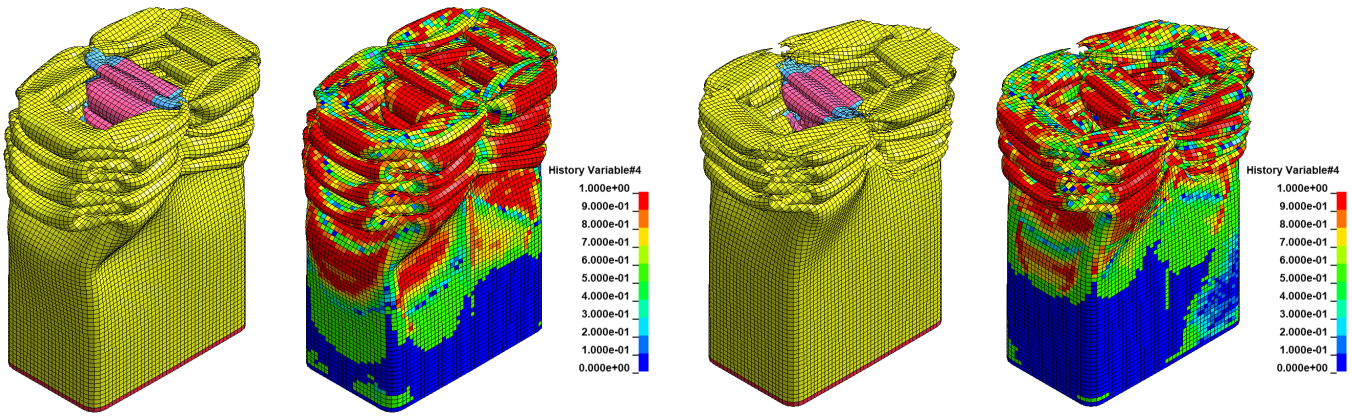

(a) Alloy A (b) Alloy B

Figure 9: Images from crush simulations with (a) Alloy A and (b) Alloy B. The fringe plots show the bending indicator Ω.

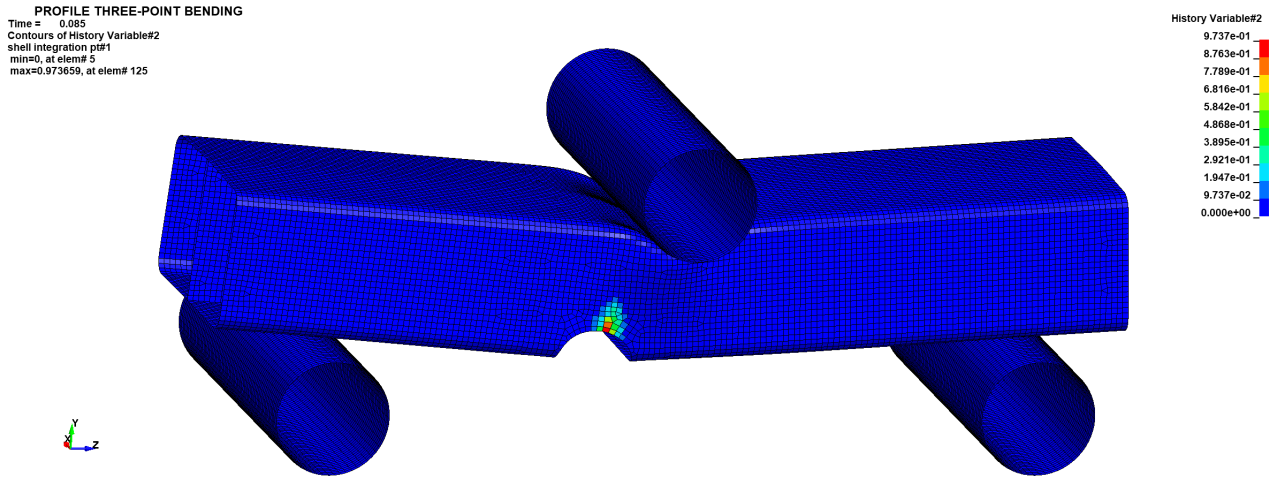

(a) Failure parameter

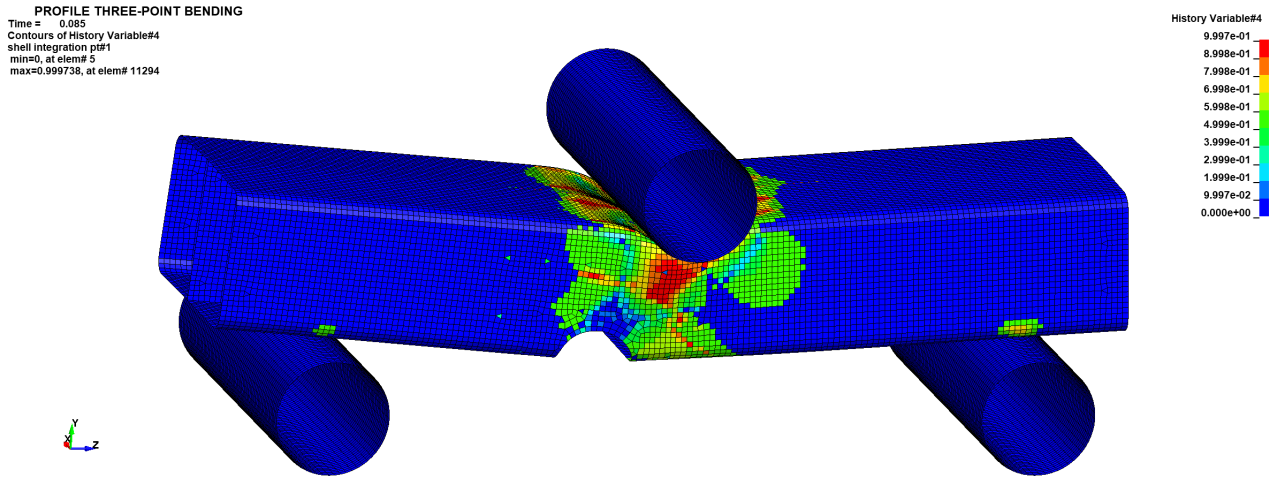

(b) Bending indicator

Figure 10: Images from three-point bending simulations with Alloy A. (a) Failure parameter and (b) bending indicator.

The CL failure criterion accounts for both stresses and strains, meaning that the point of fracture is influenced by the stress history in each element. By for instance tilting the punch slightly, perturbing the width of the web, adding geometrical imperfections, or using material parameters found specifically for the web we can change the shape of the force-displacement curves and obtain slightly more accurate fracture predictions. A simpler solution is to make changes in the element formulation. Figure 13a shows what happens with the three-point bending simulation if we use the fully integrated shell formulation in ELFORM = 16 or if we change the shell normal update option to IRNXX = -2. Now the force level increases and the displacement at fracture decreases.

Conclusions

The overall conclusion from this work is that *MAT_258 (*MAT_NON_QUADRATIC_FAILURE) can predict the fracture behavior of extruded aluminum profiles under different loading scenarios. The correlation between simulations with various element sizes and the tests was generally good, and the same material card predicted failure initiation with reasonable accuracy in three-point bending tests as well as preventing disproportionate element erosion in the crushing tests. This is of high importance for accurate assessments in design for industrial applications.

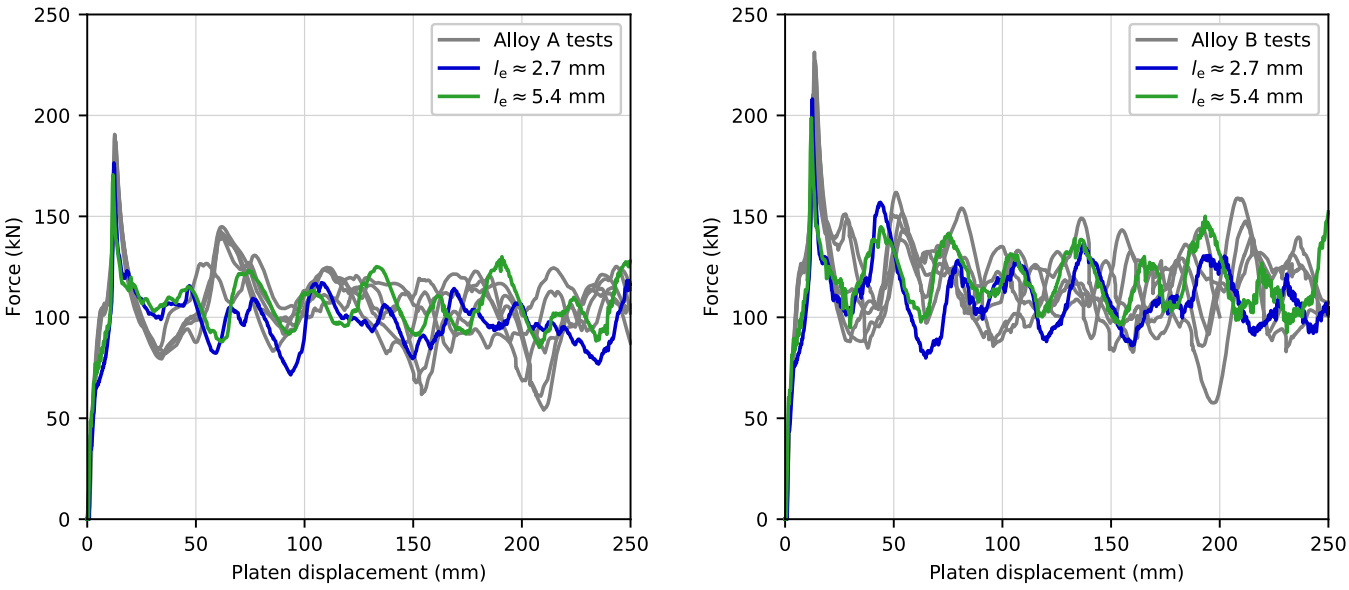

(a) Alloy A (b) Alloy B

Figure 11: Simulation results from crush simulations for (a) Alloy A and (b) Alloy B.

Two different aluminum alloys were applied in this study. Another alloy was used in the original paper by Costas et al. [1]. *MAT_258 have also been validated for Docol 1400M, a martensitic high-strength steel, in Johnsen et al. [10].

Calibrating material cards can be time consuming and expensive. An advantage with *MAT_258 is that it requires only between one and three tests for calibration, depending on the complexity of the desired fracture curve. It can also rather easily be calibrated from existing engineering stress-strain curves (also without DIC measurements).

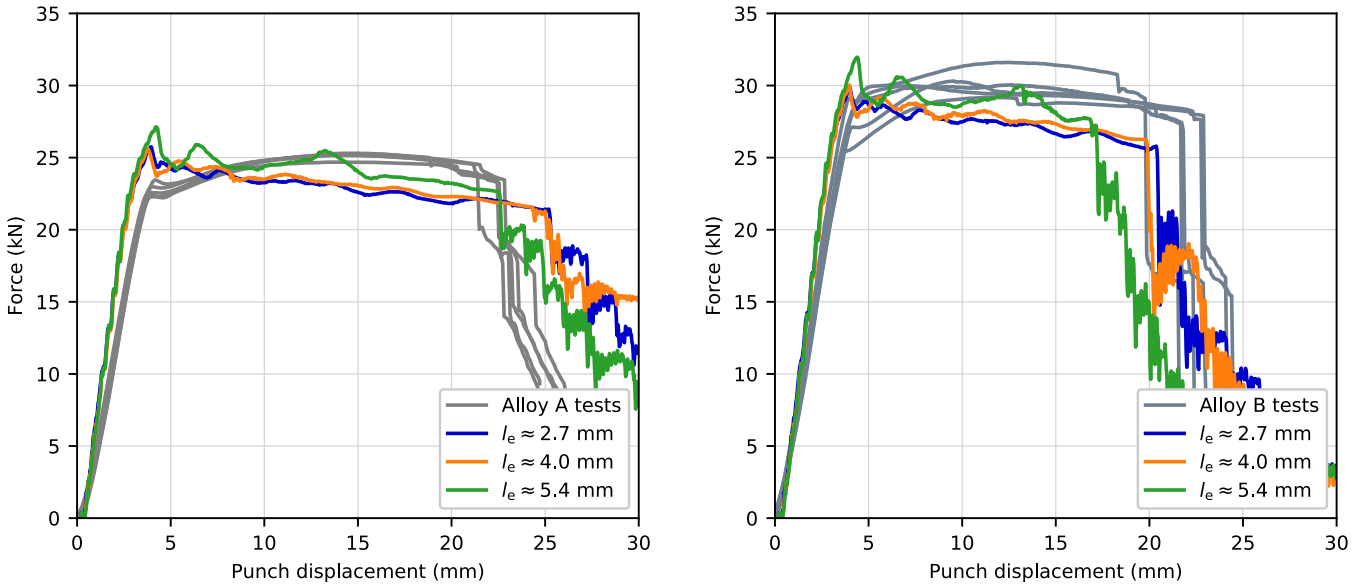

(a) Alloy A (b) Alloy B

Figure 12: Simulation results for three-point bending simulations for (a) Alloy A and (b) Alloy B.

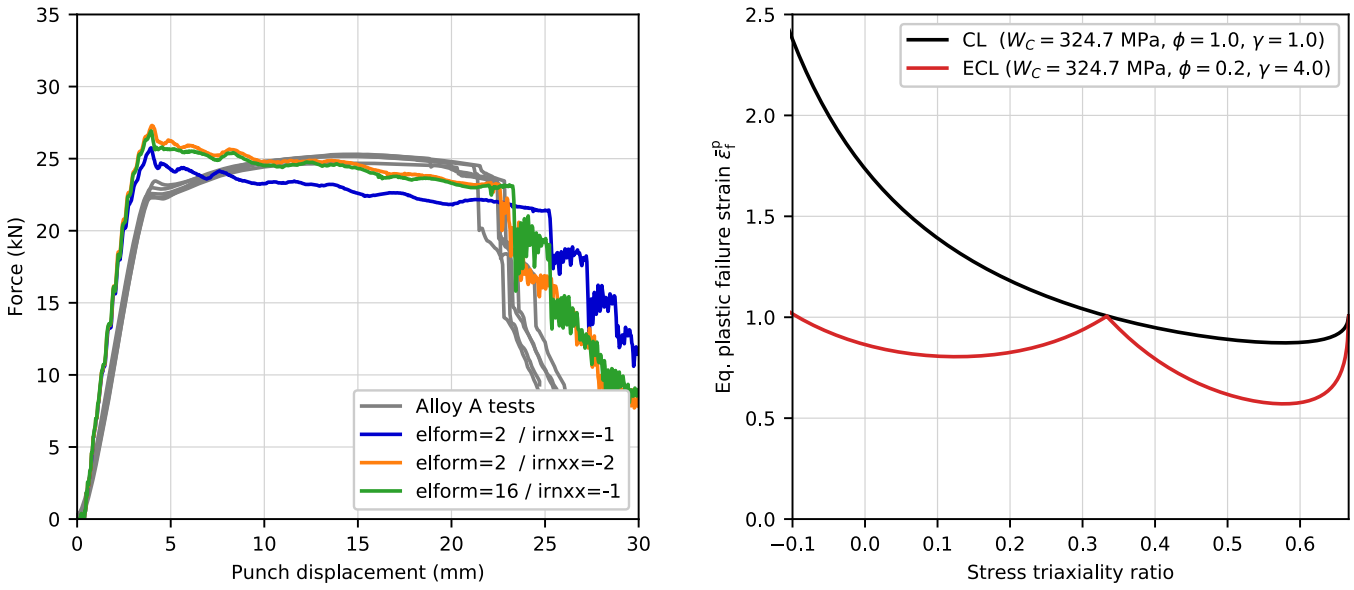

(a) Alloy A (b) Alloy B

Figure 13: (a) Effect of element size and control settings for the three-point bending test and (b) example of the more advanced fracture curve shape available by using the three-parameter ECL criterion.

For a variety of applications, this model gives equally good results to more complex models. However, the current version lacks flexibility to tackle advanced issues like plastic anisotropy and anisotropic fracture. Regardless, the model appears accurate enough, since correct control settings (IRNXX, SSTHK, etc.) and choices of element are just as important as employing a more complex material and fracture model.

As a last note, by using two additional tests, for instance a shear test and a notched tension test, we can calibrate the full ECL fracture criterion. This will improve the shape of the fracture curve and we obtain a shape as shown in Figure 13b which resembles the familiar Hosford-Coulomb, Modified Mohr-Coulomb and the standard GISSMO fracture curves.

Table 1: Material constants and work hardening parameters

	ρ (kg/m^3)	E (MPa)	ν	σ_0 (MPa)	θ_1 (MPa)	Q_1 (MPa)	θ_2 (MPa)	Q_2 (MPa)	θ_3 (MPa)	Q_3 (MPa)
Alloy A	2700.0	70000.0	0.3	255.0	69.45	1.9	57.0	1.6	1320.6	67.8
Alloy B	2700.0	70000.0	0.3	317.0	333970.0	5.5	1251.6	44.7	40.0	346.8

Table 2: Failure parameters for *MAT_258

	D_{crit}	W_C^{b} (MPa)	W_C^{l} (MPa)	W_C^{s} (MPa)	ϕ	γ	c
Alloy A	1.0	324.7	29.4	80.6	1.0	1.0	0.829
Alloy B	1.0	206.9	29.9	71.4	1.0	1.0	0.821

List of history variables

For completeness, the list of extra history variables for *MAT_258 is given below. Comments in parenthesis are relevant to this paper. Courtesy of Torodd Berstad.

1: dot_p	
2: damage	(Failure indicator D)
3: elsize/thickness-1	$(l_e/t_e - 1)$
4: omega	(Bending parameter Ω)
5: Wc	(W_C calculated using Eq. (5) and Eq. (7))
6: current number of iterations	
7: maximum number of iterations	
8: eps3_pl	
9: d3_pl	
10: number of substeps	
11: R_1	($R(\bar{\varepsilon}^p)$ for $i = 1$ defined in Eq. (3))
12: R_2	($R(\bar{\varepsilon}^p)$ for $i = 2$ defined in Eq. (3))
13: R_3	($R(\bar{\varepsilon}^p)$ for $i = 3$ defined in Eq. (3))
14: elsize/thickness	(Element length-to-thickness ratio l_e/t_e)
15: sigma_eq	
16: sigma_0+R	

Acknowledgment

The work was conducted by when JKH and JJ were full-time employees at NTNU. Funding came from the Research Council of Norway through the FORNY2020 program. The project was carried out with help from Hydro Extruded Solutions, Audi, and DYNAmore Nordic. We would like to acknowledge Hydro Extruded Solutions for providing the aluminum profiles that were used for the part of the project pertaining to this document. We also thank Björn Olsson and Andreas Assisi from Hydro for helpful input during the project period and with the preparation of this paper.

References

[1] Costas M, Morin D, Hopperstad OS, Børvik T, Langseth M. A through-thickness damage regularisation scheme for shell elements subjected to severe bending and membrane deformations. Journal of the Mechanics and Physics of Solids 2019; 123: 190-206.
[2] Livermore Software Technology Corporation (LSTC). LS-DYNA Keyword User's Manual.
[3] Camacho GT, Ortiz M. Adaptive Lagrangian modelling of ballistic penetration of metallic targets. Computer Methods in Applied Mechanics and Engineering 1997; 142: 269-301.
[4] Børvik T, Hopperstad OS, Berstad T, Langseth M. A computational model of viscoplasticity and ductile damage for impact and penetration. European Journal of Mechanics – A/Solids 2001; 20: 685-712.
[5] Logan RW, Hosford WF. Upper-bound anisotropic yield locus calculations assuming ‹111›-pencil glide. International Journal of Mechanical Sciences 1980; 22: 419-430.
[6] Gruben G, Hopperstad OS, Børvik T. Evaluation of uncoupled ductile fracture criteria for the dual-phase steel Docol 60DL. International Journal of Mechanical Sciences 2019; 62: 133-146.
[7] Cockcroft MG, Lathan DJ. Ductility and workability of metals. Journal of the Institute of Metals 1968; 96: 33-39.
[8] Dæhli LEB, Morin D, Børvik T, Hopperstad OS. A Lode dependent Gurson model motivated by unit cell analyses. Engineering Fracture Mechanics 2018; 19: 299-318.
[9] DYNAmore and DYNAmore Nordic. Recommendations for structural impact. Available from: https://www.dynasupport.com/howtos/general/recommendations-for-structural-impact [Accessed 15 March 2019].
[10] Johnsen J, Holmen JK, Gruben G, Morin D, Langseth M. Calibration and Application of GISSMO and *MAT_258 for Simulations using Large Shell Elements. 16th International LS-DYNA Users Conference. Detroit, USA. 2020.